INTAN Jurnal Penelitian Tambang
Journal Homepage : www.jurnal-intan.ac.id
e-issn: 2723-2727, p-issn: 2655-3473
OPEN ACCESS

MINERALOGY AND CHLORITE CHEMISTRY CONSTRAINTS ON THE FORMATION CONDITION OF PROPYLITIC ALTERATION IN THE TUJUH BUKIT PORPHYRY DEPOSIT, EAST JAVA, INDONESIA

POR Vannak[1*], Arifudin Idrus[1], Nugroho Imam Setiawan[1], Ryohei Takahashi[2], Ran Takeda[2], Miftahul Abrar[2]

[1] Department of Geological Engineering, Faculty of Engineering, Universitas Gadjah Mada, Indonesia
[2] Department of Earth Resource Science, Faculty of International Resource Sciences, Akita University, Japan
*Corresponding author: porvannak@mail.ugm.ac.id

ARTICLE INFO

Article history:
Received 20th June 2025
Received in revised from 6th October 2025
Accepted 12th October 2025
Available online November 2025

Keywords:
Chlorite Geothermometer
Oxygen Fugacity
Propylitic Alteration
Sulfur Fugacity

ABSTRACT

Propylitic alteration develops chlorite, epidote, and calcite assemblages commonly found in porphyry copper–gold deposits. This study aims to understand the formation temperature, oxygen, and sulfur fugacity of chlorite, a characteristic central element of propylitic-related minerals such as epidote and calcite, using a combination of qualitative and quantitative experimental methods. The propylitic alteration forming condition was analyzed in detail using a superprobe (JXA-iSP100) and Electron Probe Micro Analysis (EPMA) at a voltage of 15.0 kV. The chlorite composition is relatively homogeneous, and displayed as Mg-rich chlorite (Type-I) within Al^{IV}*-Mg-Fe, ripidolite with respect to Si vs Fe/(Fe+Mg). The chlorite geothermometer indicates that the crystallizing temperature ranges from 288.30 to 332.82°C. The oxygen and sulfur fugacity log* fO_2 *and log* fS_2 *of chlorite are low ranges (-70.4 to -51.85 and (-32.55 to -20.65), respectively. The analyses identify the mineral as true epidote, with spatial variations indicating Fe occurs as* Fe^{3+} *and Mn as* Mn^{2+}*. However, the examined proportion of moles of the significant elements (Mg, Ca, Fe, Mn) indicates that calcite is present in hydrothermal systems.*

How to Cite This Article: POR Vannak. dkk (2025). Mineralogy and Chlorite Chemistry Constraints on the Formation Condition of Propylitic Alteration in The Tujuh Bukit Porphyry Deposit, East Java, Indonesia. *INTAN: Jurnal Penelitian Tambang*, 8(2), 52–63. https://doi.org/10.56139/intan.v8i2.314

INTRODUCTION

Chlorite is a clay mineral that occurs in various geological settings, including sedimentary rocks, low-grade metamorphic rocks, and altered rocks resulting from hydrothermal processes. It can form by replacing earlier (typically iron-and magnesium-rich) minerals or by precipitating directly from fluids [1]. The system's chemistry, oxygen fugacity, and temperature and pressure conditions control the chemical composition of chlorite, a phyllosilicate, which remains stable at temperatures ranging from 80°C to over 700°C [2]. Epidote is a visually distinctive component of propylitic alteration, typically formed at $T > 2800°C$. The spatial extent of chlorite defines the outer limit of the epidote subzone, but occurrences of chlorite also extend into the actinolite subzone. It may locally overprint potassic alteration in the core of the deposit during late-stage retrograde alteration [3]. Commonly, calcite is a gangue mineral of low-sulfidation epithermal deposits, occurring as replacement calcium-bearing minerals, volcanic glass, open-space, and propylitic alteration [4]. Many researchers have studied chlorite chemistry globally, including the application of chlorite thermometry to estimate formation temperatures, the temperature and oxygen activity conditions of chlorite formation, and low-temperature chlorite geothermometry [2], [5], [6]. Moreover, Pacey (2020) investigated epidote chemistry in the porphyry ore system of Australia and epidote geochemistry in the porphyry Cu-Au deposit of China [7]. Furthermore, the development of textures and trace element signatures in hydrothermal calcite provides evidence for the ore-forming environment in Finland [8].

The discovery of the world-class Cu-Au deposit at Tujuh Bukit, East Java (1.9 Gt at 0.45% Cu and 0.45 g/t Au), has reinforced the eastern Sunda arc as a significant metallogenic belt that is highly promising for the discovery of substantial porphyry deposits. The arc hosts three premier porphyry Cu-Au deposits at Batu Hijau, Elang, and Tujuh Bukit (>300 t Au and >5 Mt Cu). Porphyry Cu-Au deposits of the eastern Sunda arc are spatially associated with small, nested, dioritic to tonalitic intrusive complexes with low-K calc-alkaline to weakly alkaline signatures [9].

The Tujuh Bukit Project is situated in Sumberagung Village, Pesanggaran District, Banyuwangi Regency, East Java Province, Indonesia. It lies approximately 60 km southwest of Banyuwangi, the regional center of the regency, and roughly 205 km southeast of Surabaya, the provincial capital of East Java. Researchers have interpreted the mineralization in the Tujuh Bukit prospect as a tonalitic porphyry Cu–Au–Mo system accompanied by a high-sulfidation Cu–Au–Ag sulfide and Au-Ag oxide cap [10].

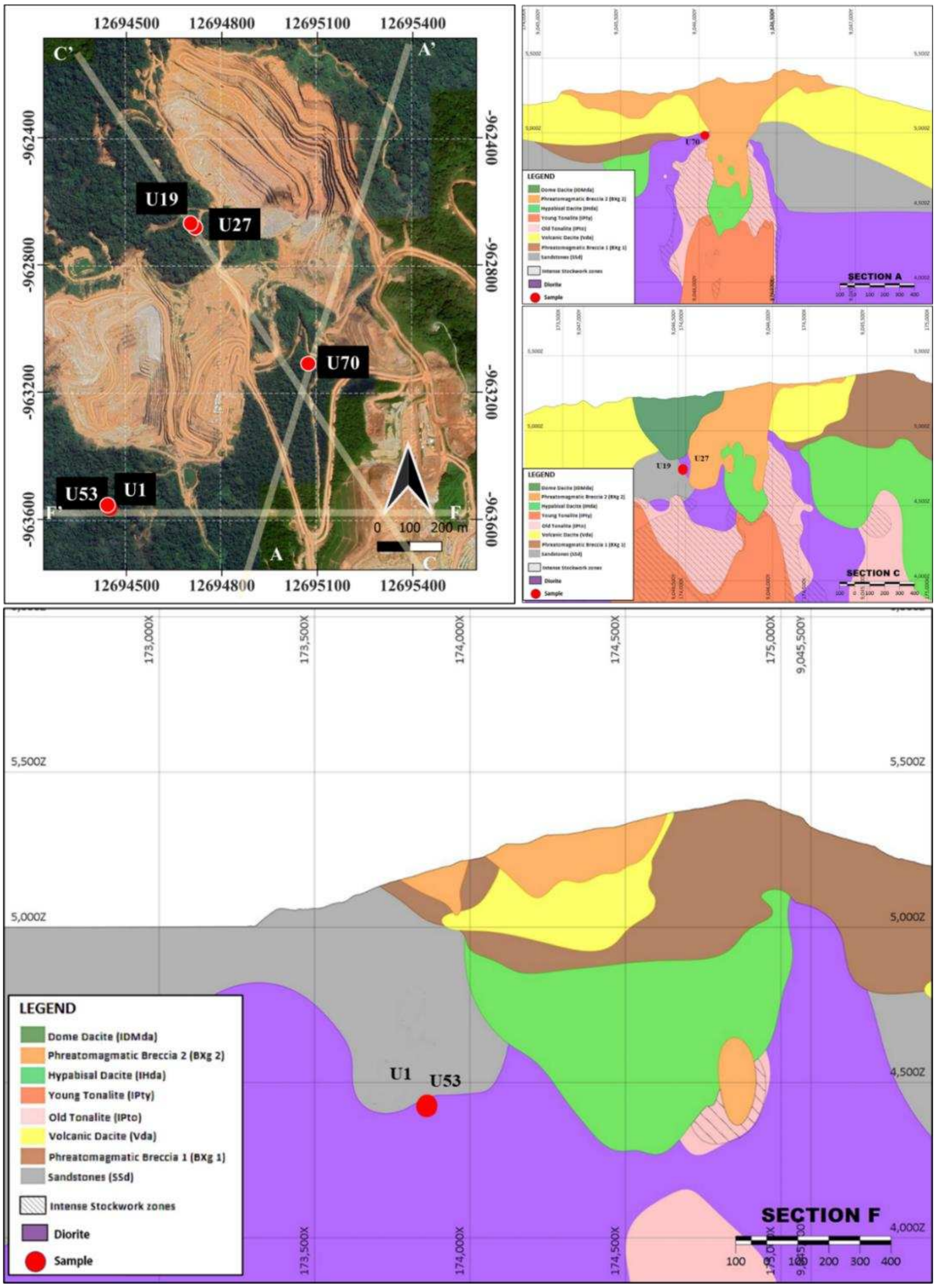

Figure 1. Location of the study area and sample selection. All samples are diorites selected from sections A-A' (U70), C-C'(U19, U27), and F-F'(U1, U53).

This study aims to understand the characteristics of minerals related to propylitic alteration (chlorite, epidote, calcite), including their classification, crystallization temperature, and oxygen and sulfur fugacity, in the Tujuh Bukit porphyry Cu-Au deposit.

RESEARCH METHODS

Sample Selection and Preparation

In this case study, we used both qualitative and quantitative experimental methods. Initially, core logging is essential for recording preliminary data such as lithology, alteration, color, and mineralization. We selected five diorite samples for petrographic thin-section preparation and electron probe microanalysis (EPMA) to characterize alteration minerals and determine the major-element compositions of specific minerals, including chlorite, epidote, calcite, magnetite, and pyrite. We prepared four samples for petrographic analysis at the Obsidian Laboratory in Bandung, Indonesia. We analyzed the remaining two samples using a super probe (JXA-iSP100) operated at 15.0 kV at the Engineering Research and Innovation Center (ERIC), Faculty of Engineering, Universitas Gadjah Mada, Indonesia.

RESULTS AND DISCUSSION

Petrography

Different mineral assemblages produced distinct types of hydrothermal alteration, influenced by variations in temperature, pressure, host rock lithology, and fluid composition. In diorite samples U19_UHGZ-23-143A, U58_UHGZ-19-009, and U70_UHGZ-22-087 from the study area, alteration minerals commonly associated with quartz, sericite, and opaque minerals indicate phyllic alteration (Figure 5.1a, c, d). In contrast, sample U1_UHGZ-23-149, an older tonalite, contains abundant calcite associated with epidote, quartz, and opaque minerals, as observed under a microscope. Electron Probe Microanalysis (EPMA) of the same sample confirms this mineral assemblage. These observations suggest that the assemblage formed within a propylitic, epidote-rich outer alteration zone (Figure 5.1b).

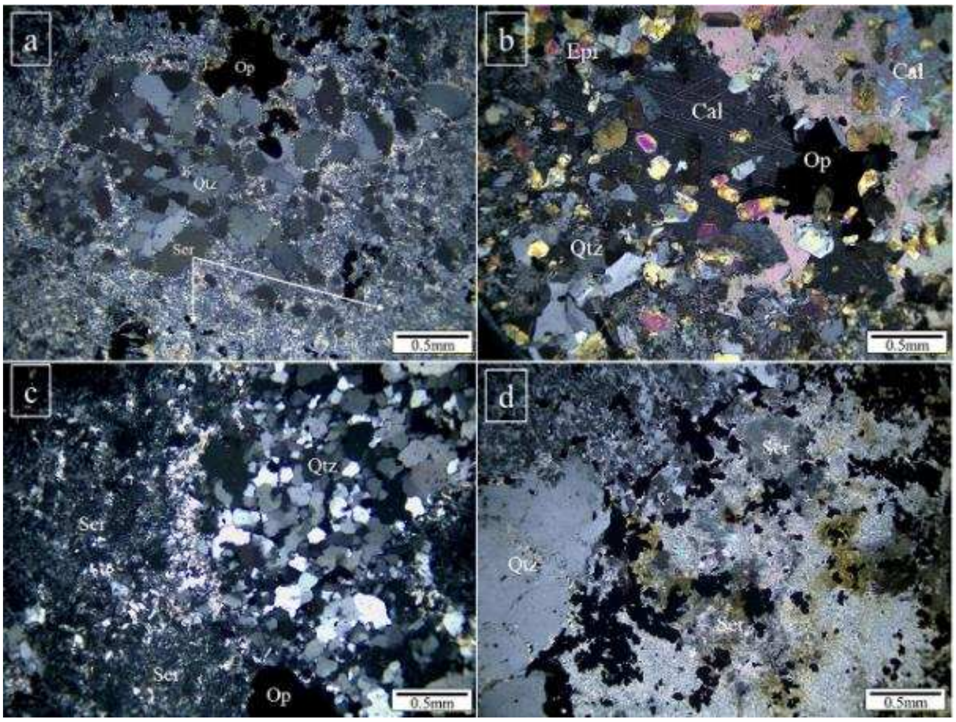

Figure 2. Photomicrographs of quartz associated with sericite, and opaque minerals (a), (c), and (d). When propylitic alteration-related minerals are dominant, calcite associates with epidote, quartz, and pyrite (b). Abbreviation: Qtz=quartz, Ser=sericite, Cal=calcite, Epi=epidote, Op=opaque.

Chlorite

Chlorite alteration in outcrop is commonly blue-grey to green with the textural pattern (including massive, patchy, and breccia). Chlorite alteration typically exhibits strong schistosity, characterized by distinct cleavage. Chlorite frequently occurs as a hydrothermal alteration mineral, especially within peripheral zones characterized by propylitic alteration (e.g., porphyry and epithermal deposits) or retrograde overprinting alteration [4].

According to the Back Scatter Electron (BSE) image of sample U53_MBH-23-052, the appearance of chlorite is medium-grey with a flaky texture. The sample is composed of chlorite, chlorite+quartz+pyrite, which is likely associated with propylitic alteration [4], [11].

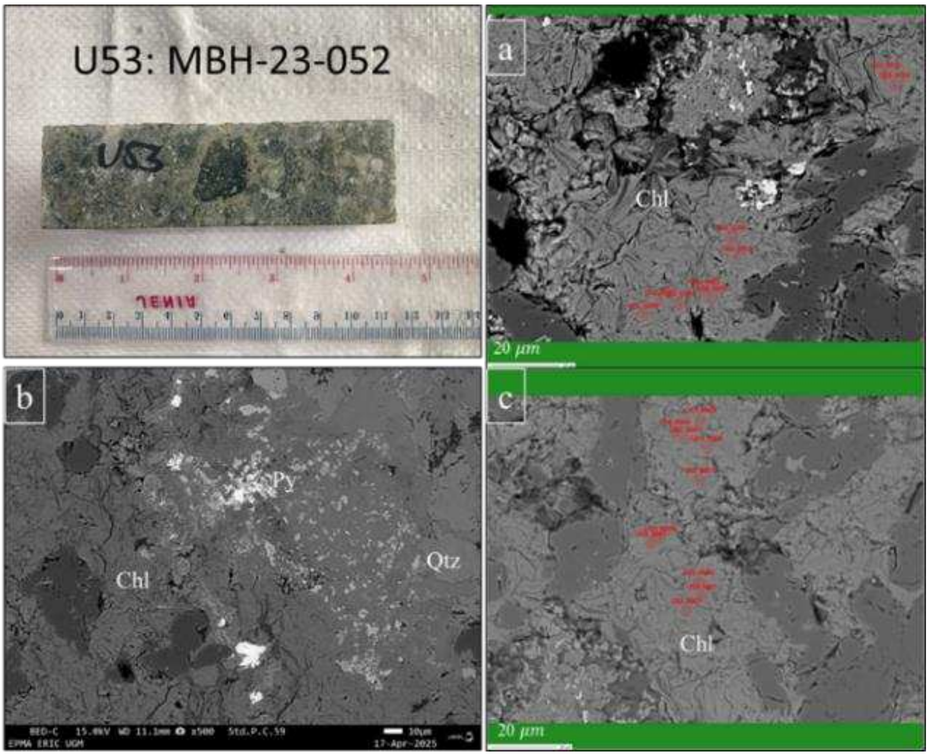

Figure 3. Back Scatter Electron (BSE) image of chlorite (red dot represents beam point analysis position). Abbreviation: Ch=chlorite, Qutz=quartz, and Py=pyrite.

Major Oxide of Chlorite and Its Classification

The chlorite composition observed was determined by EPMA using a voltage of 15.0 kV, showing that Si_2O ranges from 30.33 to 34.61 wt.%, Al_2O_3 ranges from 14.32 to 15.77 wt.%, MgO (14.25 to 18.26 wt.%), and FeO is about 21.22 to 24.25 wt.%. Some oxide elements have a lower content, such as MnO (<2.49 wt.%), CaO (<0.52 wt.%), TiO_2 (<0.03 wt.%), K_2O (<0.18 wt.%), and Na_2O (<0.12 wt.%). Alkali content ($CaO+Na_2O+K_2O$) is low, not exceeding 1 wt.% (**Error! Reference source not found.**).

Using EPMA analysis of chlorite within diorite, the structural formula was determined, assuming 36 oxygen atoms per unit cell. The data indicate that the chlorite composition is relatively homogeneous. In the Al(IV)-Mg-Fe ternary diagram [12], chlorite is plotted in the Mg-rich (clinochlore) domain (**Figure 1**a). The Si vs Fe/(Fe+Mg) classification diagram of [13] displayed the symbols of chlorite dramatically falling in and ripidolite and corundophilite (**Figure 1**b).

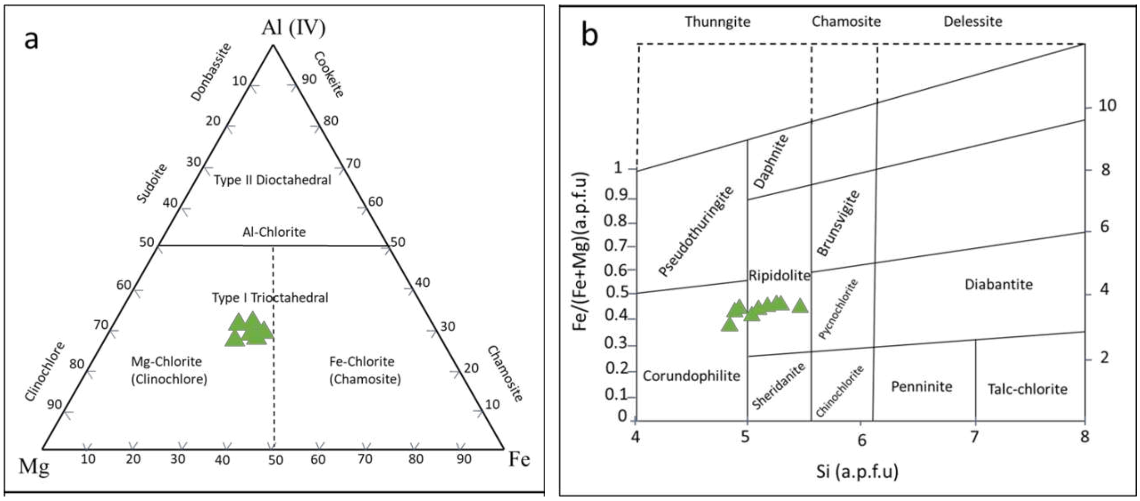

Figure 1. Classification diagrams of chlorite, showing the position of the examined sample. (a) Al (IV)-Mg-Fe, (b) Si vs Fe/(Fe+Mg) [12], [13].

Epidote

Epidote is a visually distinctive component of propylitic alteration, typically forming at temperatures greater than 280˚C. Its spatial extent defines the outer limit of the epidote subzone. At the same time, the epidote also occurs in the actinolite subzone and may locally overprint potassic alteration in the deposit core during late-stage retrograde alteration [3]. Epidote is susceptible to replacement by calcite in the presence of CO2-rich fluids [4]. The Back Scatter Electron (BSE) image shows that epidote appears white to grey (**Figure 5**a). Epidote forms clusters of subhedral crystals with a casting structure, and occurs with other calcium-bearing minerals, including calcite, quartz, and pyrite (**Figure 5**b).

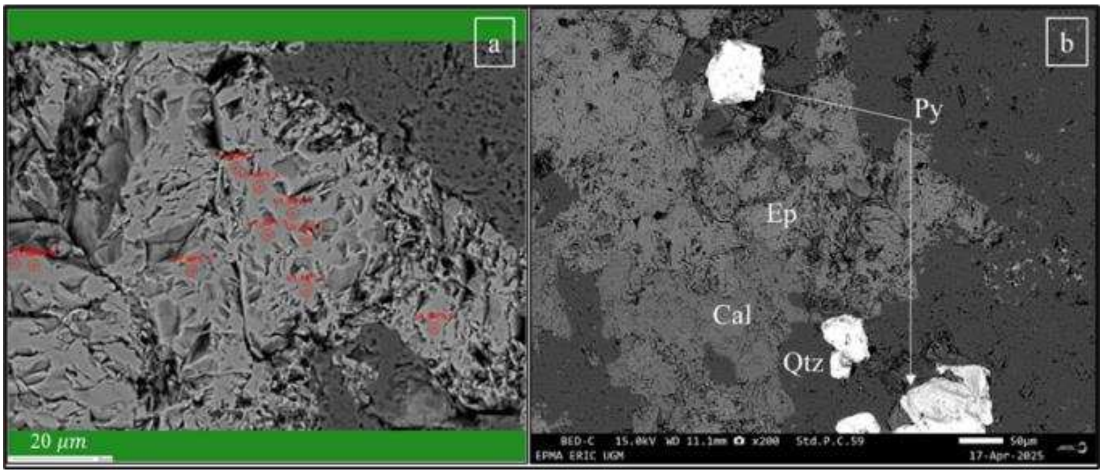

Figure 2. Back Scatter Electron (BSE) image of (a) epidote (red dots are beam point position, (b) Association of Ep+Cal+Qtz+Py. Abbreviation: Ep=epidote, Cal=calcite, Qtz=quartz, and Py=pyrite.

A Major Element of Epidote

The research team analyzed the major-element composition of epidote at the Engineering Research and Innovation Center (ERIC) of the Faculty of Engineering, Universitas Gadjah Mada. **Table 2** presents the comprehensive EPMA results for epidote. The calculations assume that all iron occurs as Fe^{3+} and normalize the data to 12.5 oxygen atoms. The result illustrates that the data classified as epidote followed the AI-2-Fe-Mn [7]. In binary plots of significant elements of epidote spatial variation, the trend association of Fe shows an excellent negative correlation with Al, whereas there is no linear correlation with Ca, Mn, or Ca+Mn (**Figure 6**b-e). The analytical results indicate that all the iron in the analyzed epidote occurs as Fe^{3+} and primarily forms a solid solution with aluminum [7], [14]. The Mn content does not display a distinct correlation with the absolute concentrations of Fe, Al, or the combined concentrations of Al and Fe; however, it shows a negative correlation with Ca (**Figures 6**f and g). The negative correlation between Mn and Ca strongly supports the occurrence of Mn as Mn^{2+}. Furthermore, the combined cation content of Ca + Mn exhibits a broad negative correlation with the sum of Fe + Al cations, suggesting an overall structural constraint of approximately 5.0 apfu (**Figure 6**h).

Calcite

Calcite is a common gangue mineral in low-sulfidation epithermal deposits, occurring as replacement calcium-bearing minerals, volcanic glass, open space, and propylitic alteration [4]. Calcite is primarily composed of Ca along with other elements, and its composition correlates with that of the surrounding country rocks. The interaction between hydrothermal fluids and the surrounding diverse host rocks has a strong influence on the trace-element composition of calcite. However, the chemical zoning observed in large calcite crystals and the presence of distinct grain populations within individual samples cannot be explained solely by host-rock control. These features instead reflect temporal variations in the composition of the hydrothermal fluids [8].

A Major Element of Calcite

The primary element composition of the hydrothermal calcite revealed CaO content ranging from 45.23 to 56.06 wt.%, indicating relatively pure calcite. These samples generally contained low levels of MgO (less than 0.23 wt.%) and FeO (below 2.74 wt.%), while MnO concentrations varied between 1.13 and 3.69 wt.% (**Table 3**).

The hydrothermal calcites from the study area are represented on a ternary diagram using the molar ratios of the key elements: Ca, Mg, Fe, and Mn. Generally, because the concentrations of Mg, Fe, and Mn in the hydrothermal calcites from sample U1_MBH-23-052 are relatively low, the data show only moderate variation. In the Ca-Mn-(Mg + Fe) diagram (**Figure 7**a), the data are aligned along several parallel trends, where Ca and (Mg + Fe) vary at a relatively constant Mn concentration (**Figure** 7b). In the Mn–Mg–Fe diagram, several calcite types align along trends with constant Mn/Fe ratios (**Figure** 7c).

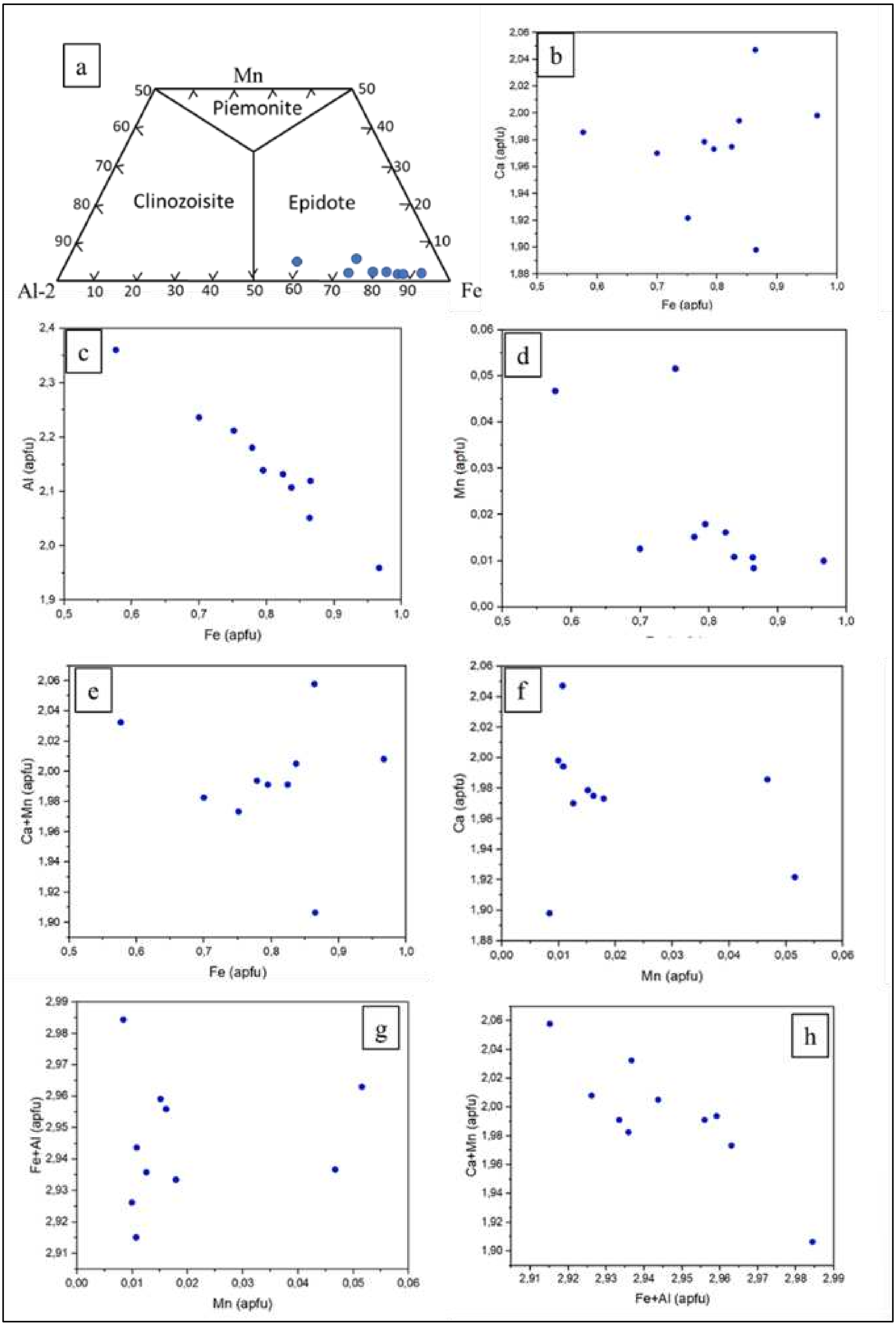

Figure 3. Diagram (a) Epidote classification diagram, (b) Major element correlation after [15].

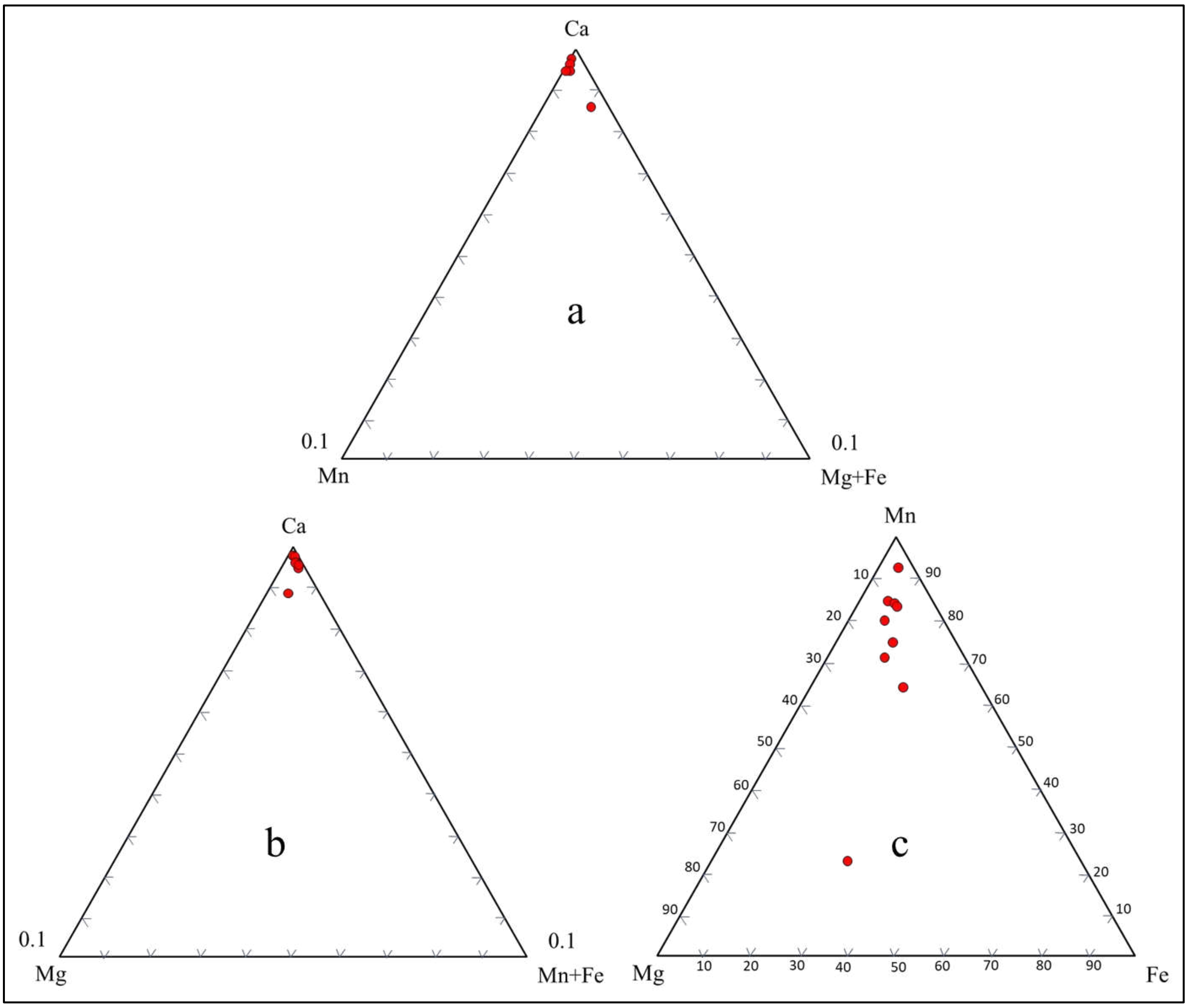

Figure 4. Ternary plots illustrate the primary element compositions of hydrothermal calcite: (a) Ca–Mg–(Mn + Fe) system, (b) Ca–Mg–(Mn + Fe), and (c) Mn–Mg–Fe [8].

Table 1. Chemical composition of chlorite in Tujuh Bukit observed by EPMA

Analysis	MP4	MP2_9	MP3_1	MP3_2	MP3_3	MP3_4	MP3_5	MP3_7	MP3_10
SiO_2	30.552	32.32	30.93	33.04	30.33	32.15	34.61	32.35	33.46
TiO_2	0,03	0,01	0	0	0	0,03	0	0	0
Al_2O_3	14.32	15.46	14.96	14.75	15.19	16.40	15.77	14.63	15.56
FeO	24.25	23.76	23.68	23.23	22.03	21.63	21.22	23.74	22.83
MnO	1.67	1.63	1.78	1.49	2.49	2.10	1.48	1.41	1.58
MgO	16.49	15.87	16.54	15.19	18.26	17.07	14.25	15.18	15.35
CaO	0.26	0.32	0.31	0.52	0.13	0.19	0.26	0.43	0.28
Na_2O	0.00	0.04	0.12	0.04	0.03	0.08	0.06	0.05	0.06
K_2O	0.10	0.12	0.05	0.14	0.05	0.08	0.34	0.14	0.18
P_2O_5	0.02	0.08	0	0.06	0.01	0.05	0.07	0.03	0.01
$CaO+Na_2O+K_2O$	0.36	0.48	0.48	0.70	0.21	0.35	0.66	0.62	0.52
Total	87.73	89.64	88.40	88.50	88.57	89.80	88.08	87.99	8.935
Number of cations based on 36 oxygens									
Si	4.94	5.10	4.95	5.24	4.83	5.02	5.44	5.17	5.25
Ti	0.00	0.00	0.00	0.00	0.00	0.00	0.00	0.00	0.00
Al	2.72	2.87	2.82	2.76	2.85	3.02	2.92	2.75	2.87
Fe^{+2}	3.28	3.13	3.17	3.08	2.93	2.82	2.79	3.17	2.99
Mn	0.22	0.21	0.24	0.20	0.33	0.27	0.19	0.19	0.21
Mg	3.97	3.73	3.94	3.59	4.34	3.97	3.34	3.62	3.59
Ca	0.04	0.05	0.05	0.08	0.02	0.03	0.04	0.07	0.04
Na	0.00	0.01	0.03	0.01	0.00	0.02	0.01	0.01	0.01
K	0.02	0.02	0.01	0.02	0.01	0.01	0.06	00.02	0.03

Analysis	MP4	MP2_9	MP3_1	MP3_2	MP3_3	MP3_4	MP3_5	MP3_7	MP3_10
OH	12.95	12.64	12.83	12.72	12.77	12.52	12.60	12.82	12.58
AlIV	2.72	2.87	2.82	2.75	2.85	2.97	2.55	2.75	2.74
XFe	0.45	0.45	0.44	0.46	0.40	0.41	0.45	0.46	0.45

Table 2. EPMA data of epidote

U1_Epidote	MP1	MP2	MP3	MP4	MP5	MP6	MP7	MP8	MP9	MP10
SiO_2	39.30	39.03	38.01	39.41	38.98	37.90	35.92	38.13	39.42	38.79
TiO_2	0.04	0.05	0.08	0.00	0.04	0.03	0.06	0.08	0.08	0.12
Al_2O_3	23.26	23.27	22.41	24.32	25.57	22.32	20.66	20.82	24.55	23.71
FeO	12.18	12.68	12.54	11.64	8.87	12.84	12.26	14.47	10.82	11.93
MnO	0.27	0.24	0.16	0.78	0.71	0.12	0.15	0.14	0.19	0.22
MgO	0.02	0.00	0.02	0.00	0.00	0.04	0.05	0.01	0.06	0.00
CaO	23.60	23.72	23.34	23.24	23.85	21.99	22.68	23.35	23.79	23.67
Na_2O	0.106	0.0	0.03	0.00	0.00	0.03	0.03	0.00	0.04	0.00
K_2O	0.00	0.00	0.00	0.00	0.01	0.00	0.04	0.00	0.00	0.00
P_2O_5	0.08	0.14	0.09	0.14	0.06	0.10	0.03	0.04	0.02	0.04
Total	98.88	99.20	96.72	99.57	98.12	95.41	91.90	97.08	99.01	98.52
Atom per formula unit based on 12,5 oxygen										
Si	3.04	3.03	3.03	3.04	3.02	3.05	3.02	3.04	3.04	3.02
Ti	0.00	0.00	0.00	0.00	0.00	0.00	0.00	0.00	0.00	0.00
Al	2.13	2.13	2.10	2.21	2.36	2.11	2.05	1.95	2.23	2.18
Fe^{+3}	0.79	0.82	0.83	0.75	0.57	0.86	0.86	0.96	0.70	0.77
Mn	0.01	0.01	0.01	0.05	0.04	0.00	0.01	0.01	0.01	0.01
Mg	0.00	0.00	0.00	0.00	0.00	0.00	0.00	0.00	0.00	0.00
Ca	1.97	1.97	1.99	1.92	1.98	1.89	2.04	1.99	1.97	1.97
Na	0.01	0.00	0.00	0.00	0.00	0.00	0.00	0.00	0.00	0.00
K	0.00	0.00	0.00	0.00	0.00	0.00	0.00	0.00	0.00	0.00
H	1.00	1.00	1.00	1.00	1.00	1.00	1.00	1.00	1.00	1.00
Al-2	0.13	0.13	0.10	0.21	0.36	0.11	0.05	-0.04	0.23	0.18

Table 3. Calcite primary element data.

Analysis Code	Weight (%)					Mol (%)				
	MgO	MnO	CaO	FeO	Total	Mg	Mn	Ca	Fe	Mn+Fe
MP3_1	0.06	3.69	56.06	0.13	59.94	0.00	0.15	2.84	0.01	0.15
MP3_2	0.14	1.69	52.37	0.16	54.36	0.01	0.07	2.91	0.01	0.08
MP3_3	0.23	1.8	52.48	0.29	54.8	0.02	0.08	2.89	0.01	0.09
MP3_4	0.07	1.41	53.14	0.14	54.76	0.01	0.06	2.93	0.01	0.07
MP3_5	0.15	2.84	51.51	0.23	54.73	0.01	0.12	2.85	0.01	0.13
MP3_6	0.13	2.7	52.79	0.24	55.86	0.01	0.12	2.86	0.01	0.13
MP3_7	0.16	1.59	52.13	0.25	54.13	0.01	0.07	2.91	0.01	0.08
MP3_8	0.16	1.15	52.55	0.34	54.2	0.01	0.05	2.92	0.01	0.07
MP3_9	2.7	2.13	45.23	2.74	52.8	0.21	0.10	2.57	0.12	0.22

Propylitic Alteration Forming Condition

Chlorite geothermometer

Numerous studies have proposed that the chlorite geothermometer can be estimated using primary element data from EPMA analyses. Researchers have developed several empirical chlorite geothermometers that rely on the ionic composition within the chlorite crystal structure [1], [2], [6]. Initially, the study indicates that the formation temperature influences the polytype of chlorite, the contents of Fe, Mg, Al^{IV}, and octahedral vacancies of chlorite, and subsequently [13], [16], [17] proposed an empirical chlorite geothermometer based on the correlation between chlorite crystallization temperature and Al^{IV} content. Subsequent studies have demonstrated that the chlorite crystallization temperature also depends on the Fe/(Fe + Mg) ratio, which correlates with the Al_{IV} content [17].

In this study, we employed two empirical equations to calculate the crystallization temperature, following the methods of Cathelineau (1988) and Kranidiotis and McLean (1987) [18]. Using updated chlorite analyses and fluid inclusion results from Los Azufres, together with recalculated and averaged data from the Sutton Sea reported by McDowell and Elders (1980), Cathelineau (1988) established the following temperature relationship, T (ºC) and Al^{IV}: $T = -61.92 + 321.98\, Al^{IV}$, which shows that the temperature ranges from (288.3 to 332.82ºC). It's considered only Al^{IV} content, which increases in parallel with the increase in temperature, but with a slight deviation (**Figure 8a**).

On the other hand, geothermometric estimates may overstate the chlorite crystallization temperature. To address this issue, Kranidiotis and Maclean (1987) introduced modified equation chlorite geothermometers based on Al^{IV}, which also factor in the Fe/(Fe + Mg) ratio. Regarding the histogram illustrated, that of temperature vs Fe/(Fe+Mg) (**Figure 8b**).

However, in the diagram, temperature vs Al^{IV}, both of the thermometer calculations (Cathelineau and Kranidiots & Maclean) were affected by Al^{IV} content (**Figure 7c**). Reference [16] confirms that the temperature calculated using the Cathelineau (1988) geothermometer represents the chlorite crystallization temperature (288.3 – 332.82°C).

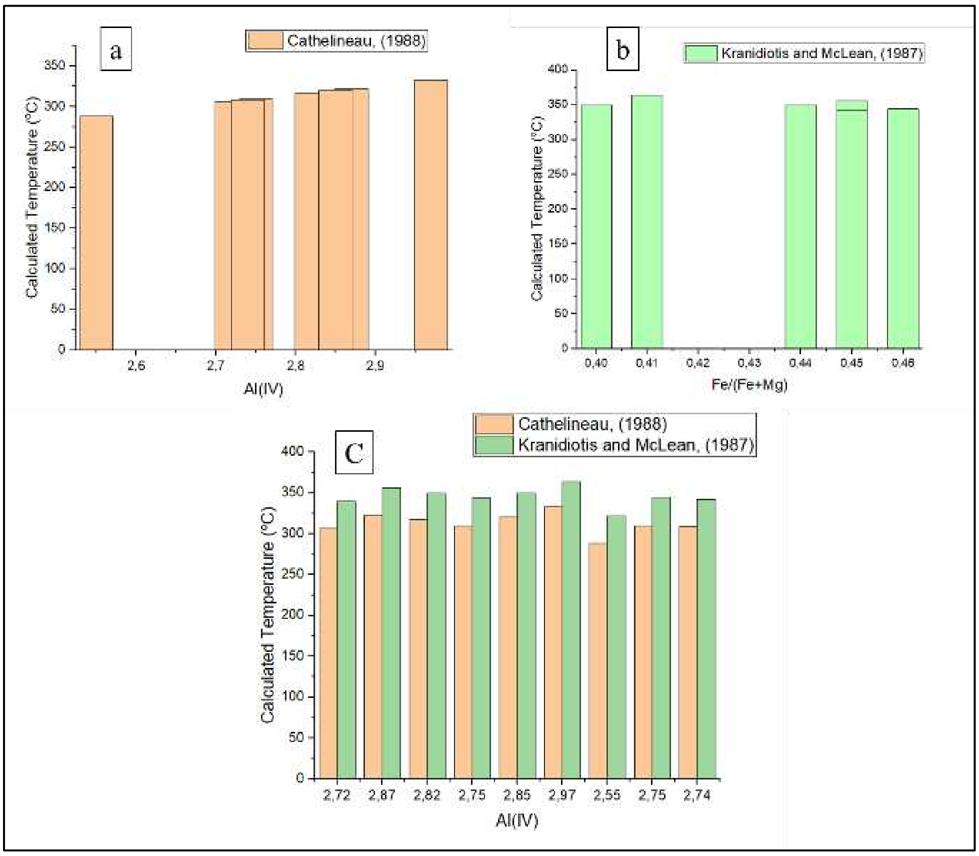

Figure 5. Distribution histogram of (a) temperature (considered Al^{IV} content) calculated by (Cathelineau, 1988) vs Al^{IV}, (b) temperature (considered Fe/(Fe+Mg) content) by (Kranidiots & Maclean,1987) vs Fe/(Fe+Mg), (c) both geothermometers considered Al^{IV} content [16], [18]

Oxygen Fugacity

The calculated oxygen fugacity [log (fO_2 /10^5 Pa)] of chlorite serves as a reliable indicator of the physicochemical conditions during its formation. Walshe (1986) and Reference [20] proposed two methods to estimate oxygen fugacity (fO_2) conditions. Some datasets are valuable because they include $Fe^{3+}/\Sigma Fe$ ratios determined through Mössbauer spectroscopy and provide estimated formation temperatures [5]. Later research has examined the results in considerable depth [2], [5], [6]. Walshe (1986) proposed that oxygen fugacity (fO_2) can be evaluated using the H-deficient Fe^{3+}-chlorite endmember, expressed as $Fe_4^{2+}Fe^{3+}Al_2Si_3O_{11}(OH)_7$, within the chlorite solid-solution system. Nevertheless, traditional electron microprobe methods are not sufficient to accurately identify this H-deficient Fe^{3+}-chlorite component [5]. According to Walshe (1986), oxygen's fugacity was calculated in the software Minpet2.0 [21].

Table 4 presents the calculated log fO_2 values plotted against the formation temperature under the vapor–liquid equilibrium pressure of water (P_{sat L/V}). The scatter diagram indicates that chlorite (U53_MBH-23-052) has a high fO_2 oxygen fugacity, corresponding to a fall in the magnetite field (**Figure 9**). The pyrite–pyrrhotite–magnetite equilibrium lowers the log fO_2 relative to the hematite–magnetite buffer and seems to regulate the prevailing redox environment in [5], Chlorite occurring alongside magnetite in veins contained higher Fe^{2+} concentrations compared to chlorite associated with hematite or occurring independently [5].

Table 4. Chlorite geothermometer.

Sample:		U53_MBH-23-052			
Rock Type:		Diorite			
Alteration:		Propylitic alteration			
N0.	Code	Log fO_2	Log fS_2	Calculated Temperature	
				Cathelineau, (1988)	Kranidiotis and McLean, (1987)
1	MP2_4	-58,49	-24,2	306,32	339,89
2	MP2_9	-62,41	-26,44	322,22	356,08
3	MP3_1	-58,18	-23,98	316,92	350,00
4	MP3_2	-70,4	-31,55	309,5	343,76
5	MP3_3	-51,85	-20,65	320,1	350,00
6	MP3_4	-58	-23,63	332,82	363,64
7	MP3_5	-69,48	-31,06	288,3	322,07
8	MP3_7	-66,03	-27,68	309,5	344,14
9	MP3_1	-67,66	-29,73	308,44	342,16

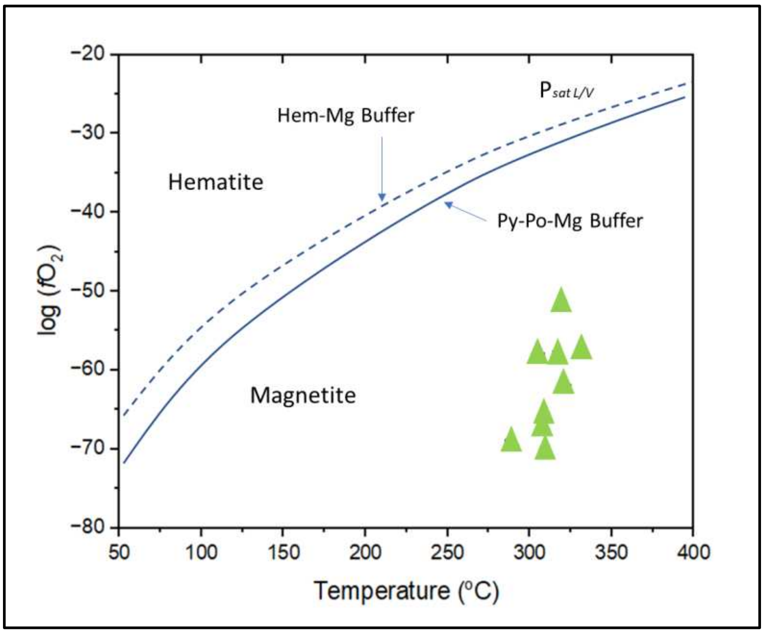

Figure 9. Estimated log fO_2 values plotted against formation temperature, calculated using the approach of Walshe (1986). The dashed and solid lines denote the hematite–magnetite and pyrite–pyrrhotite–magnetite equilibria, respectively, determined at P = Psat L/V based on the relevant thermodynamic data [5], [22]

Sulfur Fugacity

Chlorite records oxygen and sulfur fugacity, represented as log (fO_2 /10^{-5} Pa) and log (fS_2 /10^{-5} Pa), respectively, which can provide robust insights into the physicochemical environment present during its formation. The derived values (**Table 4**) show that the log (fO_2 /10^{-5} Pa) values for chlorite range between -70.4 and -51.85, with an average of -62.5, indicating formation under conditions of low oxygen fugacity (**Figure 10a**). Although the log (fS_2 /10^{-5} Pa) values of chlorite range from -32.55 to -20.65, with an average of -26.54. All projected data points plot below the buffer line, indicating formation under conditions of low sulfur fugacity (**Figure 10b**). Regarding the average of oxygen fugacity and sulfur fugacity, the type-I chlorite occurred as hydrothermal reductive related [22].

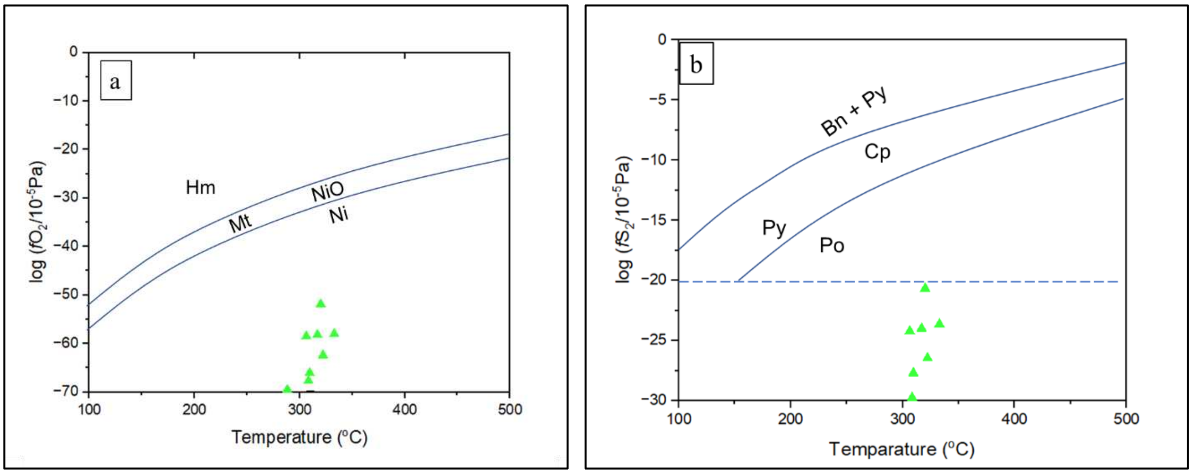

Figure 6. The logarithmic values of oxygen fugacity [log (fO_2 /10^{-5} Pa)] and sulfur fugacity [log (fS_2 /10^{-5} Pa)] buffers are plotted against temperature. A diagram showing the variation of oxygen fugacity buffers with temperature is also presented [22]. (a) The diagram of oxygen fugacity buffers as functions of temperature. (b) The diagram of sulfur fugacity buffers as functions of temperature. Abbreviation: Hm=hematite, mt=magnetite, Bn=bornite, Py=pyrite, Cp=chalcopyrite, Po=pyrrhotite, Ni=nickel, NiO=nickel oxide.

CONCLUSION

1. In the petrographic thin section, most of the samples associated with quartz+sericite+pyrite represent phyllic alteration. However, some samples dominated by chlorite, calcite, and epidote suggest the presence of a propylitic alteration zone.
2. Regarding chemical composition classification, the study classifies propylitic alteration minerals into I-type chlorite (ripidolite), true epidote, and hydrothermal calcite.
3. Chlorite crystallizes at temperatures ranging moderately from 288.3 to 332.82°C, according to the geothermometer by Cathelineau (1988), which uses Al^{IV} content.
4. The chlorite oxygen fugacity versus temperature fall in magnetite under a Py-Po-Mg buffer suggests that it is rich in Fe2+. Otherwise, the oxygen and sulfur fugacity ranges (-70.4 to -51.85) and (-32.55 to -20.65), respectively, indicate hydrothermal reduction.

ACKNOWLEDGEMENT

This paper forms part of the author's master's thesis at Universitas Gadjah Mada, supervised by the first and second authors. The research teams of UGM (Dr. Arifudin Idrus) and Akita University (Prof. Ryohei Takahashi) provided the samples used in this study through a collaborative effort. The management of the Geoscience Division at PT Bumi Suksesindo provided the core samples essential for this research, which is gratefully acknowledged.

REFERENCES

[1] P. Caritat, I. Hutcheon, and J. L. Walshe, “Chlorite geothermometry: A review,” *Clays Clay Miner*, vol. 41, no. 2, pp. 219–239, 1993, doi: 10.1346/CCMN.1993.0410210.

[2] F. Bourdelle, “Low-temperature chlorite geothermometry and related recent analytical advances: A review,” Feb. 01, 2021, *MDPI AG*. doi: 10.3390/min11020130.

[3] D. R. Cooke, P. Hollings, J. J. Wilkinson, and R. M. Tosdal, “Geochemistry of Porphyry Deposits,” in *Treatise on Geochemistry: Second Edition*, vol. 13, Elsevier Inc., 2013, pp. 357–381. doi: 10.1016/B978-0-08-095975-7.01116-5.

[4] Thomson, “geokniga-atlas-alteration,” 1996.

[5] A. Inoue, S. Inoue, and M. Utada, “Application of chlorite thermometry to

estimation of formation temperature and redox conditions," *Clay Miner*, vol. 53, no. 2, pp. 143–158, Jun. 2018, doi: 10.1180/clm 2018.10.

[6] O. Vidal, P. Lanari, M. Munoz, F. Bourdelle, and V. De Andrade, "Deciphering temperature, pressure and oxygen-activity conditions of chlorite formation," *Clay Miner*, vol. 51, no. 4, pp. 615–633, Sep. 2016, doi: 10.1180/claymin 2016.051.4.06.

[7] Q. Xiao, T. Zhou, N. C. White, S. Wang, J. Liu, and X. Li, "Epidote geochemistry of the Chating porphyry Cu-Au deposit, eastern China: Metallogenic and exploration implications for porphyry Cu deposits associated with carbonate wall rocks," *Ore Geol Rev*, vol. 179, Apr. 2025, doi: 10.1016/j.oregeorev.2025.106546.

[8] H. Kalliomäki, T. Wagner, T. Fusswinkel, and D. Schultze, "Textural evolution and trace element chemistry of hydrothermal calcites from Archean gold deposits in the Hattu schist belt, eastern Finland: Indicators of the ore-forming environment," *Ore Geol Rev*, vol. 112, Sep. 2019, doi: 10.1016/j.oregeorev.2019.103006.

[9] R. L. Harrison *et al.*, "Geochronology of the Tumpangpitu porphyry gold-copper-molybdenum and high-sulfidation epithermal gold-silver-copper deposit-Evidence for pre- and post-mineralization diatremes in the Tujuh Bukit district, Southeast Java, Indonesia," 2012.

[10] Helltman, "Intrepid Mines Limited Tujuh Bukit Project Report On Mineral Resources, Located In East Java, Indonesia Technical Report For Intrepid Mines Limited," 2012.

[11] M. Ghasemi Siani and D. R. Lentz, "Lithogeochemistry of various hydrothermal alteration types associated with precious and base metal epithermal deposits in the Tarom-Hashtjin metallogenic province, NW Iran: Implications for regional exploration," *J Geochem Explor*, vol. 232, Jan. 2022, doi: 10.1016/j.gexplo.2021.106903.

[12] Svetova, "Agates from Mesoproterozoic Volcanics (Pasha–Ladoga Basin, NW Russia): Characteristics and Proposed Origin," *Minerals*, vol. 13, no. 1, Jan. 2023, doi: 10.3390/min13010062.

[13] M. H. Hey, "the Mineralogical Magazine and Journal of the Mineralogical Society: A new review of the chlorites," 1954.

[14] A. Pacey, J. J. Wilkinson, and D. R. Cooke, "Chlorite and epidote mineral chemistry in porphyry ore systems: A case study of the Northparkes district, New South Wales, Australia," *Economic Geology*, vol. 115, no. 4, pp. 701–727, Jun. 2020, doi: 10.5382/econgeo 4700.

[15] A. Pacey, J. J. Wilkinson, and D. R. Cooke, "Chlorite and epidote mineral chemistry in porphyry ore systems: A case study of the Northparkes district, New South Wales, Australia," *Economic Geology*, vol. 115, no. 4, pp. 701–727, Jun. 2020, doi: 10.5382/econgeo 4700.

[16] Y. Feng *et al.*, "Chlorite mineralogy, geochemistry and exploration implications: A case study of the Xiaokelehe porphyry Cu-Mo deposit in NE China," *Ore Geol Rev*, vol. 140, Jan. 2022, doi: 10.1016/j.oregeorev.2021.104568.

[17] Y. Wang, H. Fan, Y. Pang, and W. Xiao, "Geochemical Characteristics of Chlorite in Xiangshan Uranium Ore Field, South China and Its Exploration Implication," *Minerals*, vol. 12, no. 6, Jun. 2022, doi: 10.3390/min12060693.

[18] F. Bourdelle, T. Parra, C. Chopin, and O. Beyssac, "A new chlorite geothermometer for diagenetic to low-grade metamorphic conditions," *Contributions to Mineralogy and Petrology*, vol. 165, no. 4, pp. 723–735, Apr. 2013, doi: 10.1007/s00410-012-0832-7.

[19] F. Bourdelle, "Low-temperature chlorite geothermometry and related recent analytical advances: A review," Feb. 01, 2021, *MDPI AG*. doi: 10.3390/min11020130.

[20] O. Vidal, P. Lanari, M. Munoz, F. Bourdelle, and V. De Andrade, "Deciphering temperature, pressure and oxygen-activity conditions of chlorite formation," *Clay Miner*, vol. 51, no. 4, pp. 615–633, Sep. 2016, doi: 10.1180/claymin. 2016.051.4.06.

[21] I. Lajtos *et al.*, "Performance evaluation and optimization of the MiniPET-II scanner," *Nucl Instrum Methods Phys Res A*, vol. 707, pp. 26–34, 2013, doi: 10.1016/j.nima.2012.12.079.

[22] D. Wu, J. Pan, F. Xia, G. Huang, and J. Lai, "The mineral chemistry of chlorites and its relationship with uranium mineralization from huangsha uranium mining area in the middle nanling range, SE China," *Minerals*, vol. 9, no. 3, Mar. 2019, doi: 10.3390/min9030199.